Research in Astronomy and Astrophysics, 24:095001 (21pp), 2024 September https://doi.org/10.1088/1674-4527/ad6a39

Spectroscopic Observations of Ten Galactic Wolf–Rayet Stars at Bosscha Observatory: Determination of Stellar Parameters and Mass-loss Rates

Hakim Luthfi Malasan[1,2] and Bakuh Danang Setyo Budi[2,3]
[1] Department of Astronomy, Faculty of Mathematics and Natural Sciences, Institut Teknologi Bandung, Bandung 40132, Indonesia; malasan@itb.ac.id
[2] Bosscha Observatory, Institut Teknologi Bandung, Lembang 40391, Indonesia
[3] Master Program in Astronomy, Faculty of Mathematics and Natural Sciences, Institut Teknologi Bandung, Jl. Ganesha No. 10, Bandung 40132, Indonesia
Received 2024 June 8; revised 2024 July 6; accepted 2024 July 23; published 2024 August 22

Abstract

We present optical spectra of 10 Galactic Wolf–Rayet (WR) stars that consist of five WN and five WC stars. The optical observation was conducted using a low-resolution spectrograph NEO-R1000 ($\lambda/\Delta\lambda \sim 1000$) at GAO-ITB RTS (27.94 cm, F/10.0), Bosscha Observatory, Lembang. We implemented stellar atmosphere Postdam Wolf–Rayet (PoWR) grid modeling to derive stellar parameters. The normalized optical spectrum can be used to find the best model from the available PoWR grid, then we could derive stellar temperature and transformation radius. To derive luminosity, stellar radius and color excess, we conducted a Spectral Energy Distribution (SED) analysis with additional data on the near-ultraviolet spectrum from the International Ultraviolet Explorer (IUE) database, and *UBV* and 2MASS *JHK* broadband filter data. Additional analysis to derive asymptotic terminal wind velocity was conducted from the P-Cygni profile analysis of the high-resolution IUE ultraviolet spectrum. With previously derived parameters, we could determine the mass loss rate of the WR stars. Furthermore, we compared our results with previous work that used PoWR code and the differences are not more than 20%. We conclude that the PoWR spectral grid is sufficient to derive WR stellar parameters quickly and could provide more accurate initial parameter input to the PoWR program code.

Key words: stars: massive – stars: mass-loss – stars: Wolf-Rayet – stars: atmospheres – stars: winds – outflows

1. Introduction

Wolf–Rayet (WR) star which is in the last stage of the evolution of a massive star exhibits a unique continuum and emission lines when compared to other astronomical objects. The continuum has a peak in the extreme ultraviolet (EUV) region which indicates that the temperature of this star is very high, similar to an O star (Willis & Wilson 1978). Furthermore, the existence of emission lines that are not like normal stars which have absorption features usually indicates that the atmospheric envelope of this star is much larger than its photosphere commonly known as an extended atmosphere (Kogure & Leung 2007). The emission profile in the optical and ultraviolet (UV) regions exhibits a P-Cygni profile which indicates that its envelope is expanding with high velocity and has a large mass loss rate (Crowther 2007). These features confused astronomers at the time of their discovery because the WR spectrum could not be modeled like a normal star using the Local Thermodynamic Equilibrium (LTE) approach.

The spectral classification of WR stars could not be based on their luminosity and effective temperature, but rather on the degree of ionization of the emission lines produced in the WR extended atmosphere (Rustamov 2017). Currently, WR stars are grouped into WN, WC and WO subtypes which depend on the dominant line observed in addition to helium such as the nitrogen ionization line in WN and the carbon ionization line in WCs. Some WC stars have an O IV line observed and then separate into a new subtype, namely WO. The quantitative classification basis for these three subtypes is given by Smith et al. (1996) and Crowther et al. (1998).

In the past, the Bosscha Observatory, Lembang, has carried out studies of WR stars through spectroscopic surveys using the Bimasakti Schmidt Telescope instrument. This study is mainly to examine the population distribution of WR stars, which are young Population I stars. WR stars could be used as tracers for the presence of the spiral arms of the Milky Way galaxy (Hidayat et al. 1982). A follow-up study of WR stars was carried out by Hidayat (1995), which focused on determining the rate of mass loss and the contribution of WR cases to the enrichment of Galactic interstellar medium (ISM). A previous study by Adhyaqsa et al. (2020) using the same Postdam Wolf–Rayet (PoWR) grid model discussed the mass-loss effect of WR stars to their environment and estimated around $\sim 0.5\,M_{\odot}$ of ejected material poured annually into Galactic ISM.

The purpose of this paper is to present our data that are observed with a small-diameter telescope and NEO-R1000 spectrograph, then we were able to measure several fundamental parameters, e.g., temperature, luminosity, etc., using a

simple and publicly accessible PoWR spectral modeling grid (Gräfener et al. 2002; Hamann & Gräfener 2003; Sander et al. 2015) that could quickly and accurately derive the parameters compared to previous literature which rely on bigger and more sophisticated instruments. In this paper, we would like to emphasize the role of small-diameter telescopes (<1 m) in monitoring spectroscopic observations of WR stars. This object is interesting to study because the spectrum cannot be modeled with well-known atmospheric models for normal stars. In addition, some of our program stars show photometric variability (Lenoir-Craig et al. 2022) and it is necessary to carry out spectroscopic follow-up observations for those objects. Many Galactic WR objects are bright stars that can be observed with small instruments and are too bright to be observed with large-diameter telescopes. The wide and strong emission features make this object very suitable for observing with a spectrograph even at low resolution and observing changes in the emission lines over time.

In Section 2, we describe our optical spectroscopic observation and data reduction. In Sections 3 and 4, we describe our method to derive WR stellar parameters. We discuss our results and compare them to previous works and we give some comments on several interesting WR samples in Section 5. In Section 6, we summarize the conclusion. Additionally, we provide the result graphs of PoWR model fitting and Spectral Energy Distribution (SED) analysis in Appendices A and B, respectively.

2. Observations and Data Reduction

We carried out eight Galactic WR star optical spectroscopy observations between 2022 September and November at GAO-ITB RTS, Bosscha Observatory, Lembang. All of these objects were located spread out in the northern and southern hemispheres due to our strategic observatory location at the equator. We selected an object minimum that represents each WR subclass that has sufficient brightness for our instrument. We were using an NEO-R1000 spectrograph ($\lambda/\Delta\lambda \sim 1000$ with a slit with of 5″) equipped with an SBIG ST-8XME CCD as the main detector and QHY174 GPS CMOS camera as the slit viewer attached to a Celestron C11 (27.94 cm, $F/10$) Schmidt-Cassegrain telescope. The Novae and Emission line Objects *R*1000 (NEO-R1000, Malasan et al. 2016) spectrograph is one of the results of a collaboration between ITB and Kyoto Sangyou University (KSU) in 2015. This compact and fast-response spectrograph has a wavelength range of $\lambda\lambda$ 3500–8000 Å and is equipped with additional peripherals of Fe–Ne–Ar hollow cathode tubes (HTC) as comparison lamps. On-chip binning of 1×2 was set throughout the observation. Additionally, we took two spectra (WR78 and WR79a) from the GAO-ITB RTS NEO-R1000 spectrum database, which were observed in June 2019, to represent a sample star from the WN7 and WN9 subclasses. All of the targets are listed in Table 1.

Table 1
Observation List

Program Stars				Spectrophotometric Standards	
WR	**ID**	**Sp. Typ**	***V* (mag)**[a]	**ID**	**Sp. Typ**[b]
6	HD 50896	WN4-s	6.94	HR 3454	B3 V
14	HD 76536	WC7	9.42	HR 3454	B3 V
16	HD 86161	WN8h	8.44	HR 3454	B3 V
23	HD 92809	WC6	7.07	HR 3454	B3 V
24	HD 93131	WN6ha	9.67	HR 3454	B3 V
78	HD 151932	WN7h	6.49	HR 7001	A0 V
79a	HD 152408A	WN9h	8.23	HR 7001	A0 V
90	HD 156385	WC7	6.92	HR 7001	A0 V
103	HD 164270	WC9d	6.61	HR 7001	A0 V
111	HD 165763	WC5	5.29	HR 7001	A0 V

Notes.
[a] van der Hucht (2001).
[b] Bright Star Catalog (5th edition).

The raw spectrum was reduced with CCDRED to produce a clean two-dimensional (2D) spectrogram, then we used TWODSPEC to produce a one-dimensional (1D) spectrum and ONEDSPEC to produce a wavelength and flux-calibrated spectrum. All of these packages were provided in IRAF.[4] The atmospheric transmittance and the response function of the instrument were calibrated with the spectrophotometric standard star and mean extinction curve of Bosscha Observatory (Malasan & Raharto 1993; Malasan et al. 2020). For the wavelength calibration, Fe–Ne–Ar spectra were obtained right before and after observations of each target star and spectrophotometric standard star. All of the spectrophotometric standard stars used for the calibration of each object are also listed in Table 1.

In the UV region, we utilized spectra provided by the Mikulski Archive for Space Telescopes[5] (MAST) from the International Ultraviolet Explorer (IUE) for additional data. We retrieved clean and calibrated low dispersion ($\Delta\lambda \sim 6$ Å) and high dispersion ($\Delta\lambda \sim 0.2$ Å) spectra using short wavelength (SWP camera, $\lambda\lambda$1150–2000 Å) and long wavelength (LWP camera, $\lambda\lambda$ 1850–3250 Å) spectrographs (Boggess et al. 1978) (listed in Table 2).

3. Stellar Atmosphere Modeling

To determine the mass loss rate parameter, spectrum modeling was performed by reproducing the observation spectrum using the PoWR code for expanding envelopes. The

[4] IRAF is distributed by the National Optical Astronomy Observatory, which is operated by the Association of Universities for Research in Astronomy (AURA) under a cooperative agreement with the National Science Foundation.
[5] see https://archive.stsci.edu/iue/.

Table 2
List of IUE Data used in this Work

WR	Low-res		High-res
	SWP	LWP/LWR	SWP
6	swp21806	lwr10476	swp43709
14	swp10712	lwr08786	swp10088
16	swp06970	lwp27144	swp13893
23	swp07027	lwr05955	swp13894
24	swp01634	lwp09539	swp01591
78	swp04335	lwr03829	swp02154
79a	swp14535	lwr11182	swp05138
90	swp25313	lwp05418	swp15130
103	swp04337	lwr03874	swp02855
111	swp02847	lwr10489	swp02872

radiation transfer equation for non-LTE environments is solved by assuming a spherically symmetric and stationary outflow that describes the velocity field (Gräfener et al. 2002). The important parameters used in this modeling are the R_t transformation radius, V_∞ asymptotic terminal velocity, $\dot{M}$ mass loss rate, L luminosity, chemical composition, D clumping factor, $R_\star$ stellar radius and $T_\star$ stellar temperature. In this atmospheric model, the inner boundary is located at a radial optical depth $\tau = 20$, which corresponds to the WR "stellar" radius $R_\star$. Then the "stellar" temperature could be defined. The transformed radius given by Equation (1) is a parameter that depends only on V_∞, $\dot{M}$ and $R_\star$. Using various combinations of values of these parameters will result in very similar emission lines as long as the R_t and $T_\star$ are the same (Gräfener et al. 2002; Hamann & Gräfener 2003; Sander et al. 2015).

$$R_t = R_\star \left[\frac{V_\infty}{2500 \text{ km s}^{-1}} \Big/ \frac{\dot{M}\sqrt{D}}{10^{-4}\ M_\odot \text{ yr}^{-1}} \right]^{2/3}. \quad (1)$$

3.1. Fitting of the Normalized Optical Spectra

The PoWR model is provided through a web interface[6] with a 2D WR spectrum grid for WN (Todt et al. 2015) and WC stars (Sander et al. 2012). These grids depend only on R_t and $T_\star$ for the WC grid and R_t, $T_\star$ and mass fraction of hydrogen for the WN grids. All other parameters in these models are made constant (see Table 3).

Determination of a suitable grid model begins by normalizing flux of the NEO-R1000 spectrum that has been dereddened with extinction data from van der Hucht (2001). Then the equivalent width (W_λ) values were measured using the SPLOT task in IRAF of some of the strong optical emission lines on WN stars such as Hα/He II 6-4, Hβ/He II 8-4, He I λ5876, He II λ5412, C IV λ5805, or O V λ5590, "diagnostic line pair" He II λ5412 and C IV λ5470, C III λ5696 and C IV λ5808 for WC stars.

In their web interface, they provided the contour map of constant equivalent widths for each emission line mentioned before. Using these contours, the appropriate area in the ($\log R_t$, $\log T_\star$) coordinate could be determined. For WN stars, there are several grid options depending on the subclasses (WNE or WNL) or the mass fraction of hydrogen (H20 or H50). In our analysis, we combine H20 and H50 models in the same area to fit with our spectrum. The best model is then chosen by taking several models around that area and then looking for the model that has the smallest χ^2 or highest R^2 parameters. The best model corresponds to the certain values of R_t and $T_\star$ (listed in Table 4). All of the spectral fits of the normalized spectrum are provided in Appendix A.

[6] This grid model is public access via https://www.astro.physik.uni-potsdam.de/~wrh/PoWR/powrgrid1.php.

Table 3
Model Grid Parameters

	WNE	WNL-H20	WNE-H50	WC
X_H	⋯	0.20	0.50	⋯
X_{He}	0.98	0.78	0.48	0.55
X_C	1.0E-4	1.0E-4	1.0E-4	0.4
X_N	0.015	0.015	0.015	⋯
X_O	⋯	⋯	⋯	0.05
X_{Fe}	1.4E-3	1.4E-3	1.4E-3	1.6E-3
$\log L [L_\odot]$	5.3	5.3	5.3	5.3
V_∞ [km s^{-1}]	1600	1000	1000	2000
D	4	4	4	10

Table 4
The Best PoWR Model for Each WR Star

WR	Sp. Typ.	Grid Model	R_t ($R_\odot$)	$T_\star$ (kK)
WN				
6	WN4-s	12–15	3.9811	89.125
24	WN6ha	H50-07-05	39.8107	50.119
78	WN7h	H50-07-06	31.6228	50.119
16	WN8h	H20-03-08	19.9526	31.623
79a	WN9h	H50-04-04	50.1187	35.481
WC				
111	WC5	10-13	6.3096	70.795
23	WC6	11-15	3.9811	79.433
14	WC7	08-12	7.9433	56.234
90	WC7	09-14	5.0119	63.096
103	WC9d	05-12	7.9433	39.810

3.2. Spectral Energy Distribution Analysis

We employed SED fitting using low-resolution NEO-R1000 and IUE low-resolution spectral data (listed in Table 2) to determine $L_\star$ and E_{B-V}. The SED profile for each model has the absolute flux $F_{\lambda,\text{mod}}$ in erg cm^2 s^{-1} Å^{-1} assuming constant luminosity for the entire model, $\log [L_{\text{mod}}/L_\odot] = 5.3$.

Table 5
Priors used to fit the UV and Optical Spectra with SED Model

Parameter	Unit	Prior Type	Value
$\log L$	$[L_\odot]$	flat	[4, 7]
E_{B-V}	[mag]	flat	[0, 1]
r	[kpc]	Gaussian	literature value
$\ln f$	⋯	flat	[−13, 1][a]

Note.
[a] Except for WR24, we used prior range [−20, 1].

The model flux is then corrected to distance and reddening dilution factor. The model flux correction is described by

$$\frac{L}{L_{\rm mod}} = \frac{F_\lambda}{10^{-0.4A_\lambda}F_{\lambda,\rm mod}} \cdot \left(\frac{r}{10\ \rm pc}\right)^2. \quad (2)$$

We used the `G16` extinction model (Gordon et al. 2016) provided by `Astropy` (Astropy Collaboration et al. 2013, 2018) assuming the Galactic reddening constant $R_V = 3.1$ and $f_A = 1$ which correspond to a purely Milky Way extinction law and values for the WR distance listed in Table 6 were taken from Gaia Data Release 3 (DR3) parallax distance (Crowther et al. 2023).

Using Equation (2), the SED fitting was performed using the Markov chain Monte Carlo (MCMC) technique with the `emcee` package in Python (Foreman-Mackey et al. 2013). We ran the MCMCs with 50 walkers for a total of 9000 steps, discarding the first 2000 steps as a conservative burn-in period. The priors used in this analysis are summarized in Table 5.

To compare the observed flux with the corrected model flux, we assumed a Gaussian log-likelihood (Equation (3)) and defined the uncertainty of the observed flux $\sigma_{F_{\rm obs}}$ as underestimated by some fractional amount f (Equation (4)).

$$\ln \mathcal{L}\,(\log L, E_{B-V}) = -\frac{1}{2}\sum_i \left[\frac{(F_{obs}(\lambda_i) - F_{mod}(\lambda_i; \log L; E_{B-V}))^2}{\sigma^2_{F_{obs}}(\lambda_i)} + \ln[2\pi\sigma^2_{F_{obs}}(\lambda_i)]\right]. \quad (3)$$

$$\sigma^2_{F_{\rm obs}} = \sigma^2_{F_{\rm UV}} + f^2 F^2_{\rm mod}. \quad (4)$$

The luminosity and reddening factor were determined by the median of the posterior distribution and 1σ uncertainty. We also show the corner plots and the 1D distributions of the posteriors of the parameters in Appendix A. All of the results are listed in Table 6.

4. Asymptotic Terminal Velocity (V_∞) and Mass-loss Rate ($\dot{M}$)

WR stars have a distinctive P-Cygni saturated line profile characterized by a flat-bottomed absorption. This line is formed at the base of the expanding envelope at a speed close to terminal velocity (V_∞) (Crowther 2007). In the UV region, several resonance lines C IV, C III and He II forming a P-Cygni saturated profile can be used to estimate terminal velocity. The P-Cygni profile would theoretically have a "blue" wing end that is a vertical edge rising from zero to the continuum, but in reality, this part will have some slope (Hillier 2020). There are two parameters that are associated with the P-Cygni profiles, namely $V_{\rm edge}$ which is the position of the wing tip of the P-Cygni profile and $V_{\rm black}$ which is the blue end of the flat-bottomed part of absorption. V_∞ was estimated from $V_{\rm black}$ (Hillier 2020) because the nonblack absorption part correlated with large random microturbulent motion gas produced by forward-propagating shocks (Prinja et al. 1990, 1991; Niedzielski & Skorzynski 2002).

In this part, we utilized the high-resolution spectrum of the IUE to calculate $V_{\rm black}$ on several highly ionized C, N, He and Si lines which formed the P-Cygni profile with almost flat-bottom absorption. $V_{\rm black}$ is determined by searching for λ with the lowest flux before rising monotonically toward the blue tip of the profile wing.

Zero reference velocity is determined depending on the shape of the P-Cygni emission line profile. If the emission profile could be estimated with a Gaussian profile, then the zero reference velocity is determined from the peak wavelength of the emission line ($\lambda_{\rm em}$). For a wide, flat-topped emission profile, the zero reference velocity is determined from the absorption line around the peak of the emission line ($\lambda_{\rm abs}$). The spectrum is assumed to be in the heliocentric reference frame (González-Riestra et al. 2000) but not corrected to stellar radial velocity. Therefore, the position of the line that is still shifting makes it difficult to determine the exact position of the zero reference velocity.

We measured the uncertainty of $V_{\rm black}$ by

$$\sigma_{v_\infty} = \frac{\bar{\Delta\lambda}/2}{\lambda_{\rm em}}c, \quad (5)$$

where $\overline{\Delta\lambda}$ is the high-dispersion average spectral resolution of ∼0.2 Å. Therefore, our analysis uncertainty is around 18–20 km s^{-1} for each line (detailed result is listed in Appendix B). Finally, v_∞ was determined through a weighted average $V_{\rm black}$ of each line, the results are given in Table 6.

Before we determine the mass-loss rate of WR stars, the stellar radius $R_\star$ must be calculated using the Stefan–Boltzman equation. If we define solar temperature of $T^N_\odot = 5772$ K (Prša et al. 2016), the calculated stellar radius of WR stars is

$$\frac{R_\star}{R_\odot} = \left(\frac{L}{L_\odot}\right)^{1/2}\left(\frac{5772\ \rm K}{T_\star}\right)^2. \quad (6)$$

In the end, with all the parameters needed already determined, we could calculate the mass-loss rate using Equation (1) with clumping factor $D = 4$ for WN stars and 10 for WC stars, as mentioned in Table 3. We employed the posterior distribution

Table 6
Comparison of Selected Derived Parameters with Literature Values

WR	Sp. Type	r	$T_\star$		E_{B-V}[a]			log L			v_∞		log $\dot{M}$			$R_\star$	M[b]	η
		(kpc)	(kK)		(mag)			($L_\odot$)			(km s^{-1})		($M_\odot$ yr^{-1})			($R_\odot$)	($M_\odot$)	
		(6)	(1)	(2)	(1)	(2)	(3)	(1)	(2)	(4)	(1)	(5)	(1)	(2)	(3)	(1)	(1)	(1)
WN																		
6	WN4-s	1.42 ± 0.10	89.125	89.1	0.16 ± 0.02	$0.13^{+0.1}_{-0.0}$	0.06	5.65 ± 0.08	$5.37^{+0.05}_{-0.04}$	5.59	2140 ± 10	2528	−4.6 ± 0.06	−4.2	−4.7	1.42 ± 0.10	18.1 ± 2.0	6.0
24	WN6ha	2.44 ± 0.20	50.119	50.1	0.23 ± 0.01	0.29 ± 0.1	0.18	5.9 ± 0.07	$6.12^{+0.07}_{-0.05}$	6.01	2090 ± 8	2194	−5.17 ± 0.06	−4.3	−4.5	2.44 ± 0.20	26.3 ± 2.7	0.9
78	WN7h	1.64 ± 0.10	50.119	50.1	0.64 ± 0.01	0.58 ± 0.2	0.51	6.25 ± 0.05	$6.03^{+0.08}_{-0.08}$	5.63	1715 ± 8	1135	−4.84 ± 0.04	−4.5	−4.4	1.64 ± 0.10	43.8 ± 3.4	0.7
16	WN8h	2.28 ± 0.10	31.623	44.7	0.69 ± 0.01	$0.74^{+0.2}_{-0.3}$	0.57	5.34 ± 0.05	$5.60^{+0.09}_{-0.10}$	5.78	1087 ± 10	676	−4.82 ± 0.04	−4.6	−4.5	2.28 ± 0.10	11.5 ± 0.9	3.7
79a	WN9h	1.65 ± 0.10	35.481	35.5	0.49 ± 0.01	0.42	⋯	5.93 ± 0.06	$5.37^{+0.05}_{-0.04}$	⋯	1689 ± 11	955	−4.94 ± 0.04	−4.6	⋯	1.65 ± 0.10	27.3 ± 2.2	1.1
WC																		
111	WC5	1.33 ± 0.10	70.795	89.0	0.31 ± 0.03	$0.42^{+0.1}_{-0.2}$	0.3	5.13 ± 0.1	$5.20^{+0.07}_{-0.07}$	5.40	1926 ± 10	2398	−5.23 ± 0.08	$-4.64^{+0.09}_{-0.08}$	−5	1.33 ± 0.10	8.4 ± 1.2	4.1
23	WC6	2.31 ± 0.10	79.433	79.0	0.57 ± 0.03	$0.74^{+0.3}_{-0.2}$	0.44	5.38 ± 0.09	$5.51^{+0.09}_{-0.10}$	5.34	2247 ± 10	2342	−4.83 ± 0.07	$-4.49^{+0.07}_{-0.06}$	−4.9	2.31 ± 0.10	12.3 ± 1.5	6.9
14	WC7	1.74 ± 0.10	56.234	71.0	0.80 ± 0.02	$0.77^{+0.3}_{-0.2}$	0.62	5.31 ± 0.07	$5.56^{+0.10}_{-0.10}$	5.19	1959 ± 9	2194	−4.94 ± 0.05	$-4.39^{+0.05}_{-0.05}$	−4.7	1.74 ± 0.10	11.1 ± 1.0	5.4
90	WC7	1.32 ± 0.05	63.096	71.0	0.41 ± 0.02	$0.48^{+0.2}_{-0.1}$	0.44	5.29 ± 0.08	$5.67^{+0.06}_{-0.07}$	5.50	2029 ± 9	2053	−4.79 ± 0.06	$-4.59^{+0.04}_{-0.04}$	−4.6	1.32 ± 0.05	10.8 ± 1.1	8.3
103	WC9d	2.52 ± 0.20	39.810	45.0	0.66 ± 0.02	$0.65^{+0.1}_{-0.2}$	0.48	5.24 ± 0.09	$5.19^{+0.09}_{-0.10}$	5.20	846 ± 6	1010	−4.91 ± 0.07	$-4.56^{+0.18}_{-0.15}$	−4.6	2.52 ± 0.20	9.9 ± 1.2	3.0

Notes.
[a] The reddening factor in references (2) and (3) were in the Smith system E_{b-v}. For comparison, we converted the value into the Johnson–Cousin system using the relations $E_{B-V} = 1.21E_{b-v}$ and $A_v = (1.12R_V + 0.36)E_{b-v}$ as described in Lundstrom & Stenholm (1984).
[b] Masses calculated from theoretical luminosity–mass relation for WR stars given by Fadeyev (2008).

References: (1) This paper (typical error for $v_\infty \sim \pm 20$ km s^{-1} and $\dot{M} \sim \pm 0.09\ M_\odot$ yr^{-1}); (2) WN: Hamann et al. (2019) except WR79a: Skinner et al. (2012), WC: Sander et al. (2012, 2019) ; (3) Nugis & Lamers (2000); (4) Nugis & Lamers (2000), except WR90: Dessart et al. (1999); (5) Niedzielski & Skorzynski (2002). ; (6) Crowther et al. (2023) except WR79a: Skinner et al. (2012).

of previous SED analysis to determine $R_\star$, $\dot{M}$ and the 1σ uncertainty. In addition, we estimated the WR mass and momentum transfer efficiency (explained in the next section) using Equations (7) and (8) respectively. All of the results are tabulated in Table 6.

5. Discussions

For most of the WN stars, the stellar temperatures derived in this work perfectly fit with previous calculations by Hamann et al. (2019), except for WR16. On the other hand, it was really difficult for us to fit WC spectra with models resulting in most of them deviating from the literature value (Sander et al. 2019) up to 20%. One possible reason we suspect is the variations in helium, carbon, oxygen and nitrogen abundances differ from those assumptions used in the PoWR grid model, resulting in no model adequately matching our observed spectrum. This discrepancy is expected as the He abundance in the WC starts to decline with the inner shell undergoing He nuclear burning approaching the WO phase. This could influence the abundance ratio of each element in the atmosphere.

Our results for SED analysis show a good fit in the UV, optical and near-infrared (near-IR) regions except for WR24 which will be explained later. The data points in the optical *UBV* and near-IR Two Micron All-Sky Survey (2MASS) *JHK* bands are slightly shifted toward stronger than the model flux. We observe that many strong emission lines are within these broadband filters, therefore the differences with the model are still within reasonable limits. However, for objects with weaker emissions, a much better fit is obtained. The luminosity we obtained is in good agreement with previous literature and we suspect the discrepancy comes from differences in the model and UV spectrum used with previous literature.

The reddening constant also in general showed a good agreement with literature values within 2σ of our result, except for WR111 which is much smaller than the literature. This is due to the presence of a lot of emission lines around λ2200 blurring the real continuum which really impacts the accuracy of our analysis. Our analysis relies on parallax distance from Crowther et al. (2023) who referenced the newest Gaia DR3 parallax data with a prior model based on H II region distribution and Galactic dust extinction model in the same was as previous analysis with Gaia Data Release 2 (DR2) (Rate & Crowther 2020). The H II region can be used to approximate the distribution of massive stars such as WR and OB cases, but the difference is not more than 5%. Another factor that we suspect is the model input as absolute flux models really depend on the model position in the log R_t, log $T_\star$ diagram. The accuracy of the reddening constant also could contribute to differences since a higher reddening constant tends to lower the model flux compared to what is observed. The differences in terminal velocity are also expected due to the method used for determining V_∞ with the P-Cygni profile, which is still limited to Gaussian fittings and "eye" measurements, making measured terminal velocity less accurate. Then for the mass-loss rate, the maximum difference is $\sim$14% for WR24 and lower for others, in spite of many uncertainties in the input parameters. We will discuss some of the interesting objects and give some comments based on our analysis below.

WR6, widely known as EZ CMa, is one of the variable WR stars that has been studied in many papers. It shows a prominent variability either in light curves, spectrum, or polarization (Hamann et al. 2006) due to its intrinsic property and not by a binary companion. A recent study of polarization on EZ CMa showed that corotating regions and wind flattening may produce changing, large-scale patterns in the stellar wind, which might lead to the variability of linear polarization with a rotational period of $\sim$3.7 days (de la Chevrotière et al. 2013).

WR14 has a photometric variability confirmed by a recent study with Transiting Exoplanet Survey Satellite (TESS) data (Lenoir-Craig et al. 2022). The previous literatures that explained the cause of variability are Bromage et al. (1982) & Shylaja (1990) which discussed the possibility of a compact companion in WR14. When we tried to fit the normalized optical spectrum to a model, no model could fit all the observed emission lines. Among these models, there are emission lines that are too strong compared to the observed ones and vice versa. Therefore, we choose the model with the best-fit parameters even though there is a C III λ5696 Å line that does not fit the model at all (see Figure A2). This is one of many factors that cause a discrepancy with previous literature values (Sander et al. 2019).

Same as WR14, WR16 was confirmed to have variability by a recent study with TESS (Lenoir-Craig et al. 2022) which is one of the possible reasons for the variability in the WR16 spectrum and causes the $T_\star$ and R_t parameters we obtained to be different from previous literature (Hamann et al. 2019). WR16 is surrounded by a bubble nebula which is expected to have X-ray emission due to shock-heated plasma as strong WR stellar winds interact with remnant ejected material when this star is in the red supergiant or luminous blue variable phase (Garcia-Segura & Mac Low 1995). However, Toalá & Guerrero (2013) showed no detection of hot plasma with XMM-Newton data. Furthermore, there is no further study to explain the causes of variability as observed from TESS data.

WR24 is one of three WR stars in the Carina Nebula star formation region (NGC 3372). When we tried SED fitting on this object with the entire data (IUE spectra and 2MASS flux), we arrived at much larger extinction values than found in Hamann et al. (2019). We also observe that the bump in λ2200 which is an important feature of interstellar extinction does not fit well with the model spectrum. Therefore, we tried to fit the SED by taking only the continuum region around λ2200, then comparing the results with the overall SED. The result of reddening is consistent with previous literature (Hamann et al. 2019) and we found clear evidence of infrared (IR) excess

which is a strong indication of the existence of a circumstellar disk around WR24. There is no previous literature that clearly mentions this, but the formation of dust around the mass-losing star is expected. Dust is observed in luminous blue variables (LBVs) that have nebulae and likely originates from large envelope eruptions or outer material swept up by strong stellar winds (Crowther 2007). The latest research on this object only mentions the possibility of hot plasma detected using XMM-Newton X-ray data. There is no indication of the presence of a companion in this object (Sasaki et al. 2024).

WR90 is a WC7 star that also has a stochastic variability in TESS photometric data (Lenoir-Craig et al. 2022). Research on this object has been carried out such as the detection of an unusual absorption line at λ2200 caused by the presence of a nebula around it (yet at that time no nebulosity had been detected around it) (Willis & Wilson 1977). Further research was carried out on the distribution of expanded neutral hydrogen gas (H I) around WR90. This H I bubble was caused by WR90 and its progenitor O class stars (Cappa de Nicolau et al. 1988). The interaction between the stellar wind and material ejected from WR90 and pre-existing supernova remnant nebula RCW 114 produces several unique features from the emission and absorption in its spectra, one of them is the NaI absorption line (Welsh et al. 2003). Same as WR14, this object has no model that could fit all the observed emission lines. In fact, when we fit spectra with the literature model, it produces an inadequate result. However, when we find the "best" model, the results strongly deviate from the literature value. This is already explained in Sander et al. (2012) such that in the WC model, some of the lines, especially C III λ4650, lines between λ6500 and 7200 Å, are not perfectly matched with observation. Therefore we chose to use the best model despite the deviation.

WR103 is another example of a WR star with significant variation in its TESS light curve (Lenoir-Craig et al. 2022). Spectroscopic observation is also conducted by Chené & St-Louis (2011) which showed an insignificant line-profile variability without a clear period. This star belongs to the WC9d stars which means WR103 is producing dust persistently which might be caused by colliding wind between WR stars and its OB companion (van der Hucht 2001). A previous study that tried to investigate the possibility of companions is Massey et al. (1984) which suggested a dust shell-like structure around WR103. There are no recent studies that demonstrated the presence of a companion for this star.

We were facing the same problem as WR14 and WR90 when we tried to fit the spectrum of WR111 to models. WR111 is one of the WC5 stars that exhibits a parameter degeneracy mentioned in Sander et al. (2012). This happens when the winds are very dense or $\log R_t \leqslant 0.4$, with some combination of different R_t and $T_\star$ which might lead to nearly the same spectrum models that made our results not well-constrained. Therefore, this might explain the differences between our results and references for this star.

At this point, we have derived six parameters of WR stars: temperature, reddening constant, luminosity, terminal velocity, and mass-loss rate. Then we chose five of these parameters to be compared with the literature values listed in Table 6. Two types of literature are used, first literature that uses the same method as our analysis, and second literature that uses a different approach to determine these parameters.

Another fundamental parameter that we could explore is WR mass. Theoretical WR mass could be determined if we know the luminosity–mass relation for WR stars. Fadeyev (2008) provides a linear fit for this relation for models with initial masses ranging within $70\,M_\odot \leqslant M_{\rm ZAMS} \leqslant 130\,M_\odot$ given by

$$\log L/L_\odot = 3.675 + 1.568 \log M/M_\odot. \quad (7)$$

There are many approaches to determining the luminosity–mass relation for WR stars. It is widely recognized that WR stars have large mass-loss rates due to stellar wind that significantly impacts their evolutionary track (Chiosi & Maeder 1986). We calculated the theoretical mass for our samples using Equation (7) (results are listed in Table 6) and then compared it to the calculated mass in Hamann et al. (2019) for WN stars and Sander et al. (2019) for WC stars. These papers use the luminosity–mass relation proposed by Langer (1989) with WNE stars corresponding to pure helium stars. WNE stars are a type of WR star that exhibits a spectrum with no hydrogen lines and very weak carbon or oxygen lines. The mass difference is up to 80% due to the different models applied and the oversimplified relation that we employed. The luminosity–mass relation depends on many factors, but mainly mass-loss rate and helium fraction (Fadeyev 2008).

We also derived another parameter that is momentum transfer efficiency η, mathematically defined as

$$\eta = \frac{\dot{M} v_\infty}{L/c}. \quad (8)$$

This wind momentum to photon momentum ratio indicates how efficiently each photon transfers momentum once to the wind, which was first proposed by Springmann (1994). The $\eta = 1$ means "single scattering limit" in which each photon transfers its momentum once to the wind. Most WR stars have $\eta > 1$ so that the driving winds of WR stars cannot be entirely explained by a single scattering. Nugis & Lamers (2000) showed that η is weakly dependent on luminosity, but mainly dependent on composition, with higher helium abundance giving a higher η.

The mass-loss rate of WR stars is expected to be strongly correlated to their luminosity since the stellar wind mechanism is driven by radiation. To investigate this, we plotted our results in the $\dot{M} - L$ plot (see Figure 1) and compared it to the

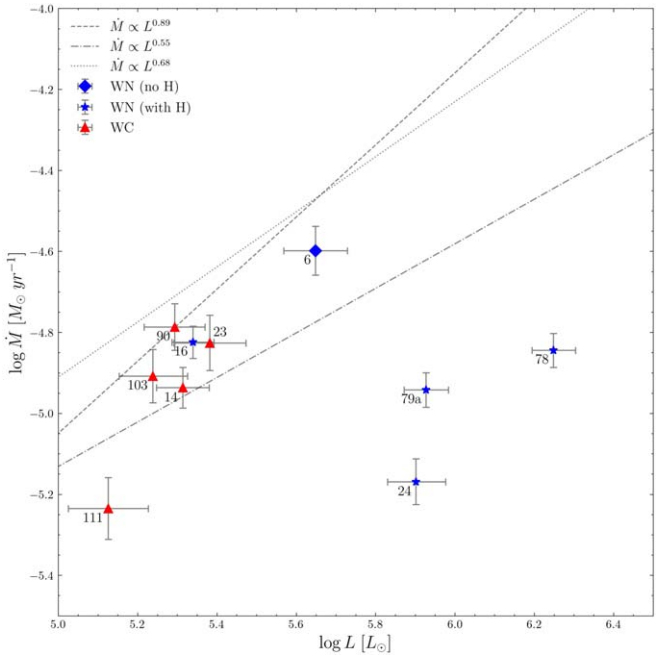

Figure 1. Mass-loss rate vs. luminosity for our Galactic WR sample stars compared to the empirical law derived in previous literature. Labels refer to WR catalog numbers. The dashed and dash-dotted lines are the linear empirical law for WN stars with no hydrogen and with hydrogen respectively given by Hamann et al. (2019). The dotted line is the linear empirical law for WC stars given by Sander et al. (2019).

correlation given by Hamann et al. (2019) for WN with hydrogen (WNh) and WN hydrogen-free stars, and Sander et al. (2019) for WC stars. The result is that our WR78 and WR24 have a much lower mass-loss rate than expected. For WR79a we could not compare with Hamann et al. (2019) because this object is not included in their samples. However, the other samples showed a good agreement with the empirical law.

In the Hertzsprung–Russell diagram (HRD), a high temperature and luminosity WR case indicates that this star is related to the late evolution stage of O stars. Conti (1975) first proposed an evolutionary scenario that allows evolved massive O stars to lose the majority of their hydrogen shells through stellar wind mechanisms. This massive mass-loss will reveal the surface of the star so that H-burning products can be observed, then followed by He-burning products. This proposed theory became known as the "Conti Scenario."

Meynet et al. (1994) showed that the progenitor O star had a minimum mass of 65–110 $M_\odot$. It is currently believed that the initial mass cutoff of WR progenitors is around 25 $M_\odot$ (Crowther 2007) or even as low as 18 $M_\odot$ which challenges our current understanding of nucleosynthesis processes in massive stars (Sander et al. 2019). The evolution scheme for progenitors with an initial mass >80 $M_\odot$ (Sander et al. 2012) states that the WC stage will not be passed so that when it enters the LBV phase and then goes to WNL, this star will go straight to SN IIn. This sequence is confirmed by observations of SN2015bh which show the LBV (Boian & Groh 2018) and SN2014C progenitors changing from SN type Ib to type IIn and signifies the presence of a hydrogen-rich outer shell which is thought to originate from the ejection of the LBV progenitor shell (Margutti et al. 2017; Brethauer et al. 2022). The O progenitor with a lower mass will go through the WC and then WO phases until the core collapses. WO is a very suitable type Ic supernova progenitor candidate because its spectrum shows depletion of hydrogen and helium (Sander et al. 2019).

In Figure 2, we present the positions of our program stars on the HRD, showing a clear grouping between WC and WN. WN samples that still contain hydrogen in their outer envelopes (WNh) tend to be on the right side of the zero-age main sequence (ZAMS) track compared to WN hydrogen-free stars (e.g., WR6 in our samples). This indicates that a hydrogen-free WN has a higher surface temperature than WNh because the deeper and hotter helium-rich layer is starting to be exposed and could be observed. In addition, this strengthens the WR evolution scheme in which a hydrogen-free WR star is the next evolutionary stage after the WNh phase before entering the WC phase.

WC stars are the result of further evolution of a hydrogen-free WN when it has lost its helium outer shell and is exposed to the helium-burning products in its atmosphere (Hamann et al. 2019). The WC stars also tend to have a lower luminosity due to their mass being increasingly eroded. In the same figure, we showed evolution tracks of various initial masses from Ekström et al. (2012) with and without initial rotation. The single-star evolution model with rotation can reach the WR region in the HRD with a smaller initial mass than the model without rotation which indicates the importance of rotation in WR progenitor evolution. However, even in this model, the minimum observed luminosity limit is $\log L/L_\odot = 5.4$ which does not explain the existence of a WC with lower luminosity, indicating that these objects require a much greater mass-loss rate in the previous evolutionary stages (Georgy et al. 2012; Sander et al. 2019).

6. Conclusions

At this point, we obtained the low-resolution optical spectra of 10 Galactic WR stars using the `NEO-R1000` spectrograph at Bosscha Observatory. Additional archival data of low- and high-resolution UV spectra are needed for stellar atmosphere modeling using `PoWR` model grid. We derived several fundamental parameters of WR stars e.g., stellar temperature, reddening constant, luminosity, terminal wind velocity, stellar radius and mass-loss rate through model fitting and SED analysis Our results in general do not perfectly match the

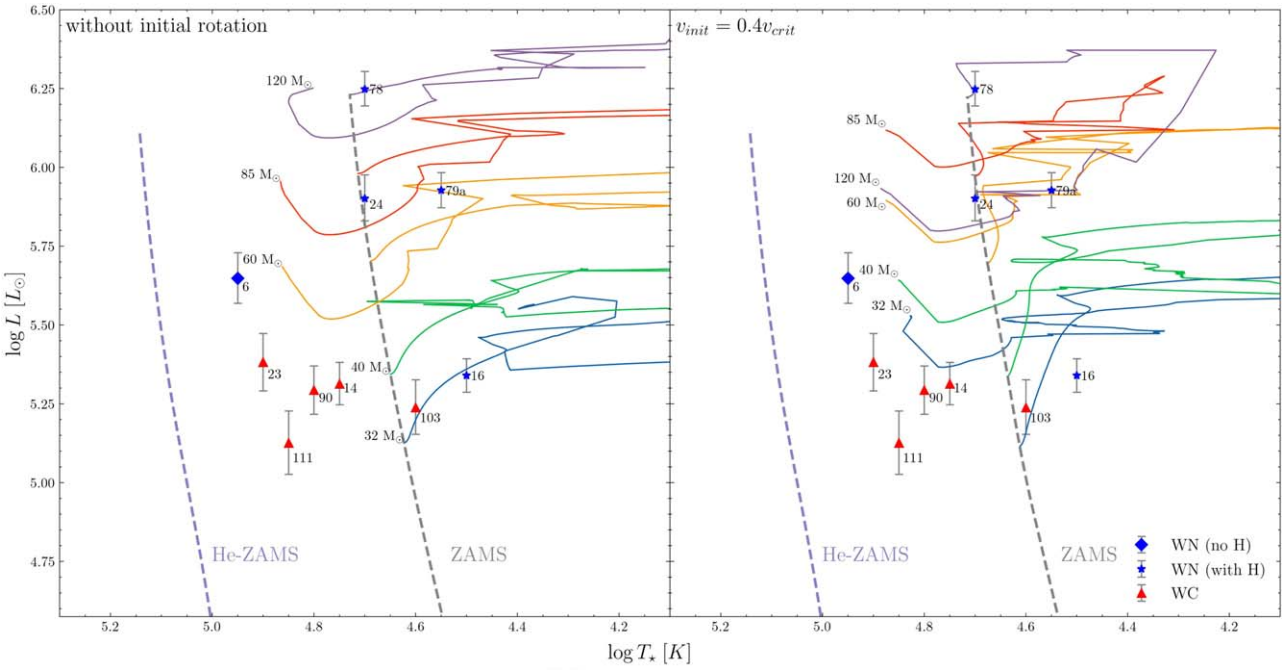

Figure 2. HRD for our program stars compared to the evolutionary tracks of single stars with no initial rotation (left panel) and $v_{\rm init} = 0.4v_{\rm crit}$ (right panel) adopted from Ekström et al. (2012). Each evolutionary track for each initial mass is given a different color with a label listed. The ZAMS tracks for solar abundance for each model from Ekström et al. (2012) and for pure helium stars (He-ZAMS) from Langer (1989) are depicted as gray and light blue dashed lines, respectively.

literature value, but are still within 20% of the maximum error for some parameters. This is quite good considering the limitations of the model that can be selected to produce a suitable fitting. This method is also very good for testing the performance of the NEO-R1000 spectrograph, which for many years has been an important instrument at the Bosscha Observatory for studying the spectroscopy of emission line objects, especially novae. The next job is considered modeling directly without using a grid spectrum and more accurate parameters will be obtained.

Acknowledgments

We would like to thank staff of Bosscha Observatory for providing support to conduct this research. We also thank the anonymous referee for their comments and some advice, which hugely improved the quality of the paper. BDSB is very grateful to Evan I. Akbar M.Sc., and Dr. Lucky Puspitarini, and Dr. M. Irfan Hakim for the ideas and suggestions that were very helpful in the preparation of this paper. This research is supported through HLM's Program Penelitian Pengabdian Masyarakat ITB (P2MI) Astronomy Division, FMIPA ITB grant 2022–2023. Some of the data presented in this paper were obtained from the Mikulski Archive for Space Telescopes (MAST). STScI is operated by the Association of Universities for Research in Astronomy, Inc., under NASA contract NAS5-26555. Support for MAST for non-HST data is provided by the NASA Office of Space Science via grant NNX13AC07G and by other grants and contracts.

Appendix A
Best Model Fitting Result

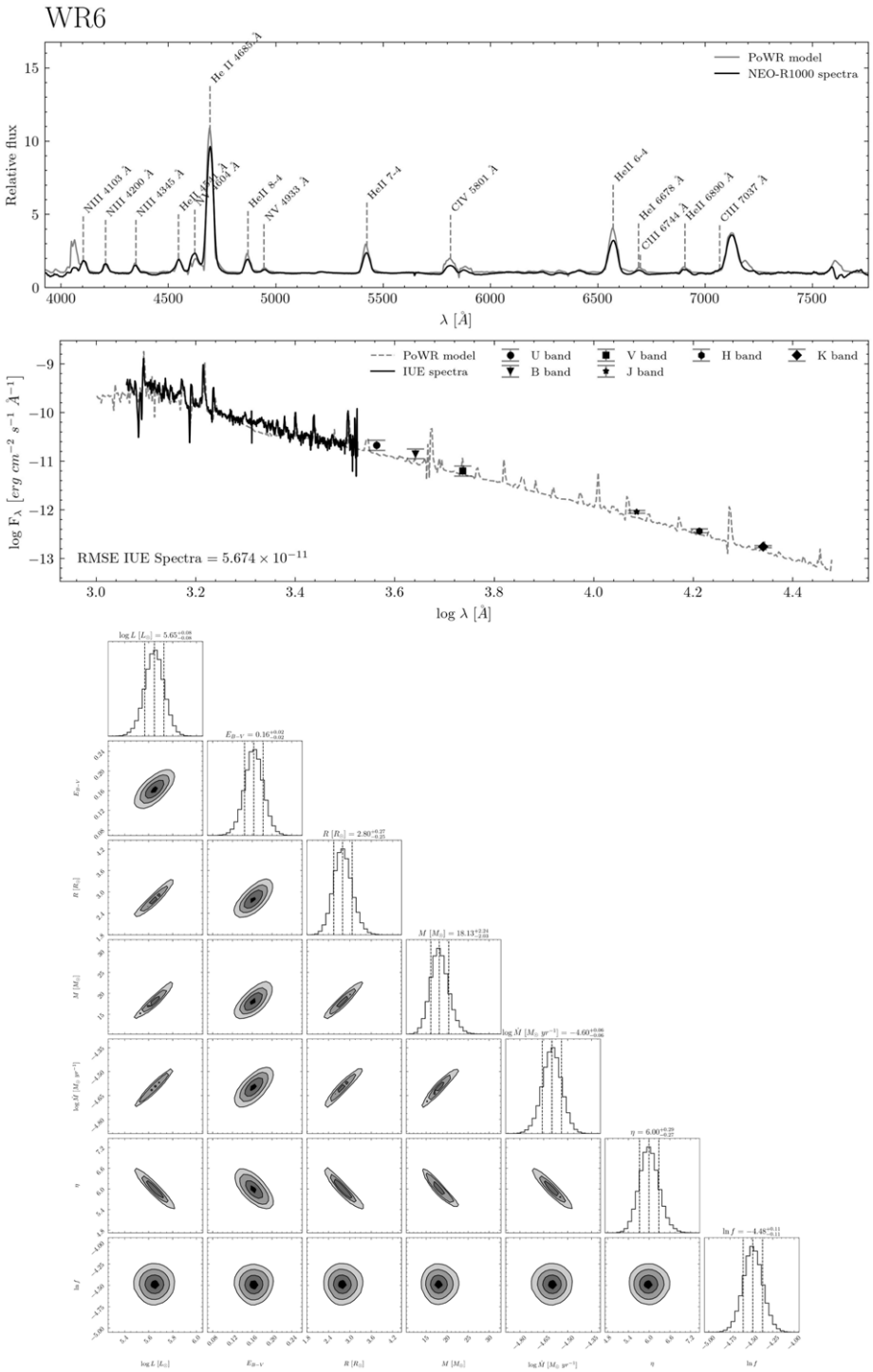

Figure A1. `NEO-R1000` optical spectral fitting for determining best model (upper panel), SED fitting using `IUE` spectra, *UBV* and 2MASS JHK_s photometry (middle panel) and the bottom panel shows the posterior distribution of SED analysis or WR6.

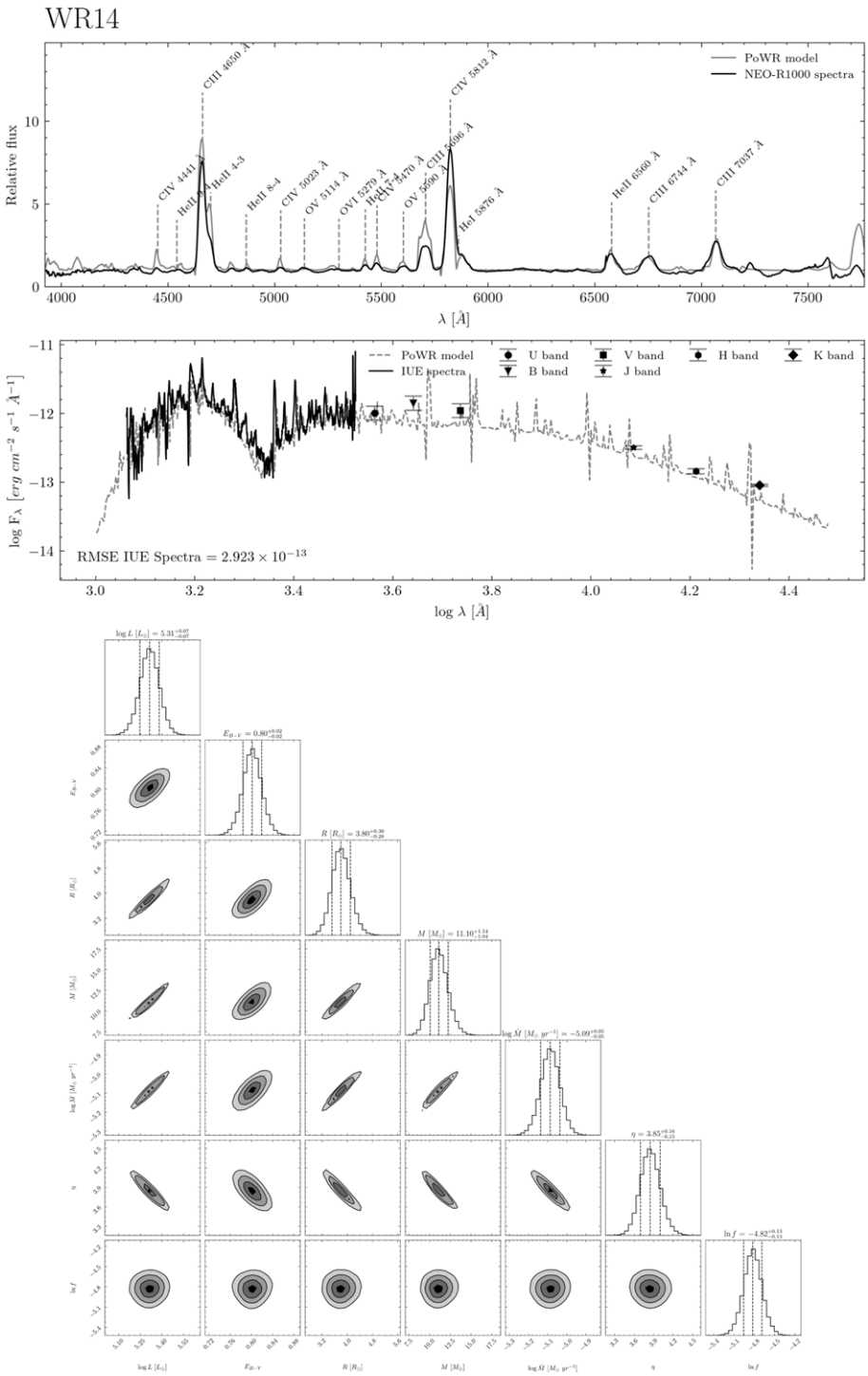

Figure A2. Fitting for WR14, same description as Figure A1.

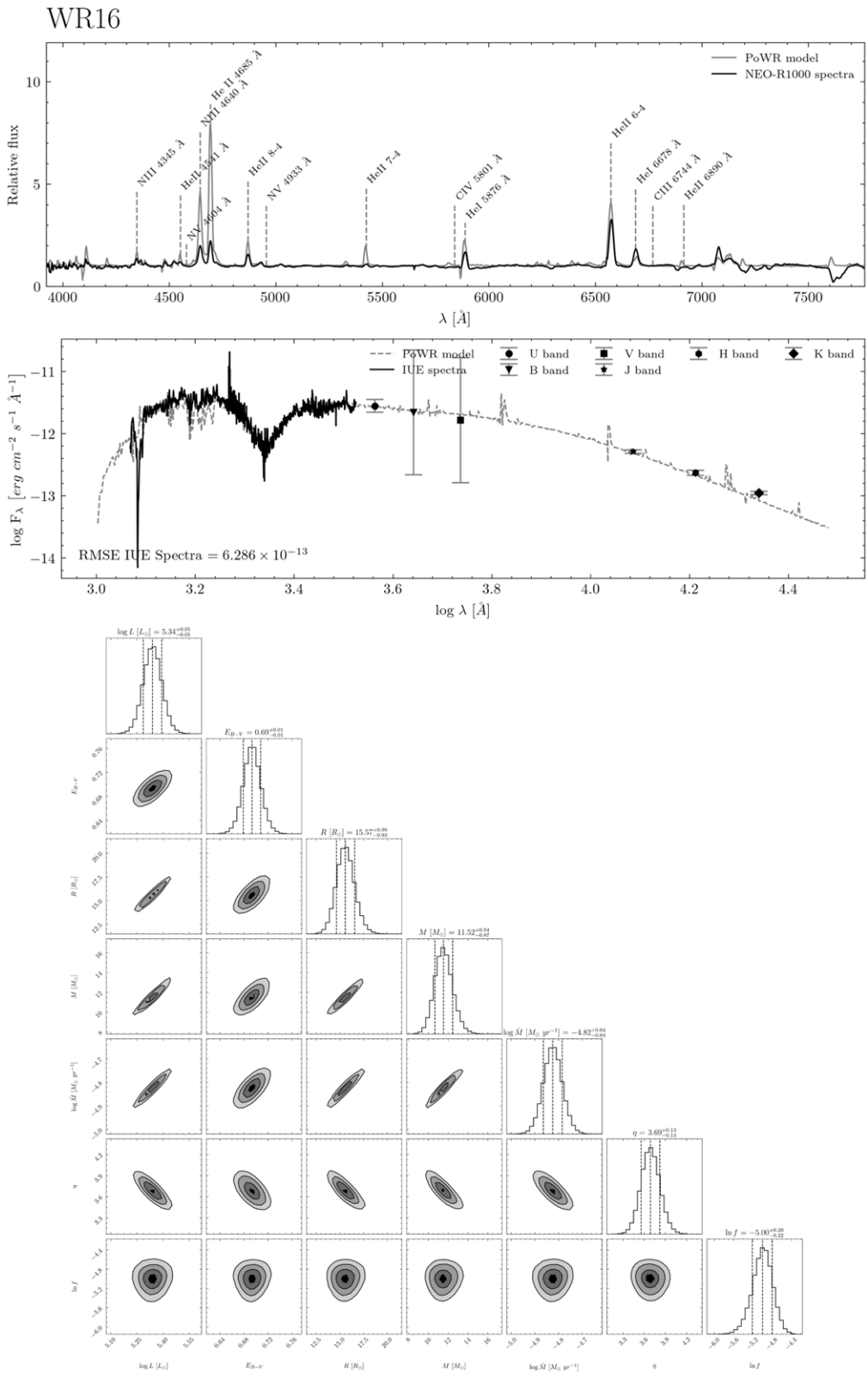

Figure A3. Fitting for WR16, same description as Figure A1.

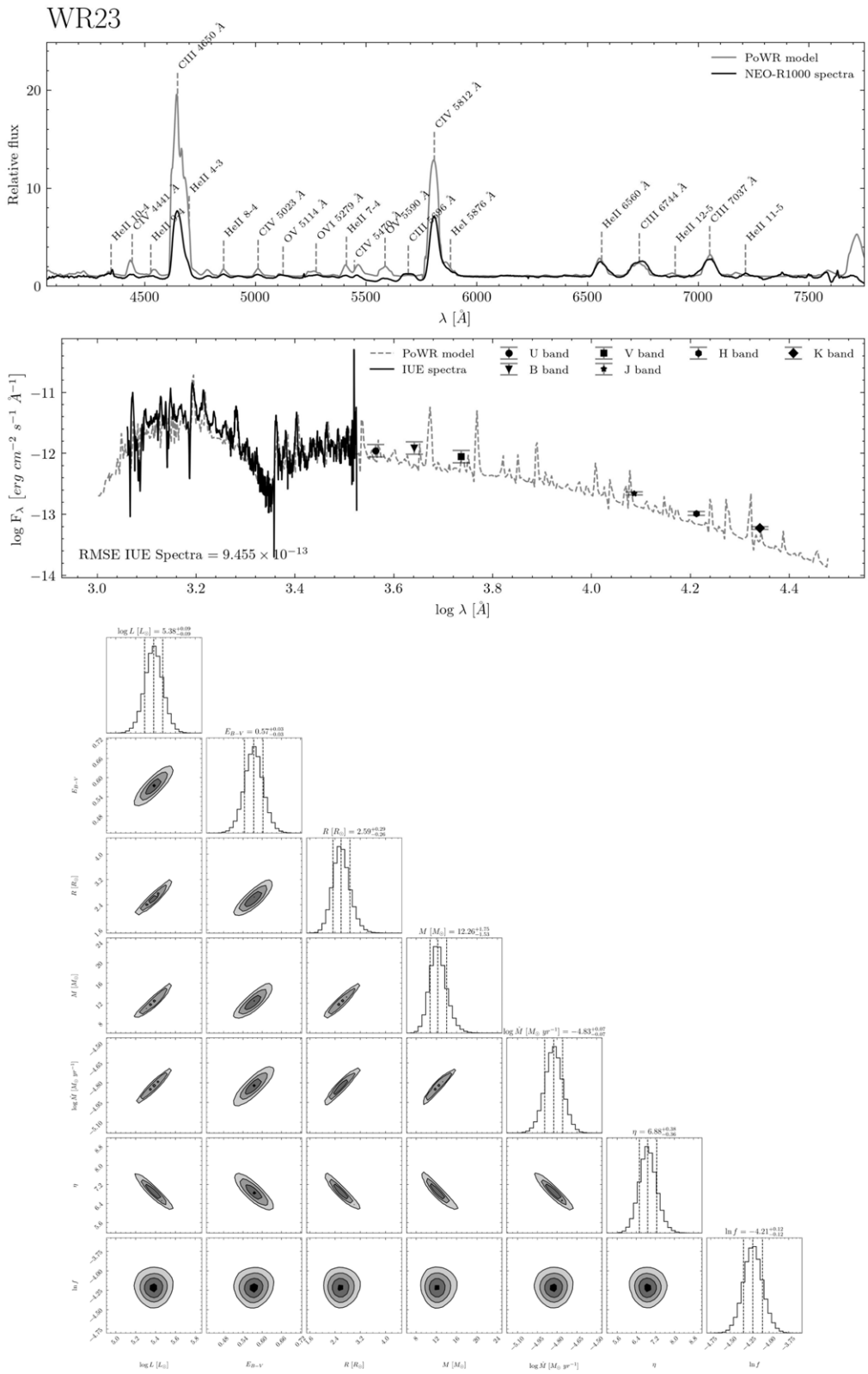

Figure A4. Fitting for WR23, same description as Figure A1.

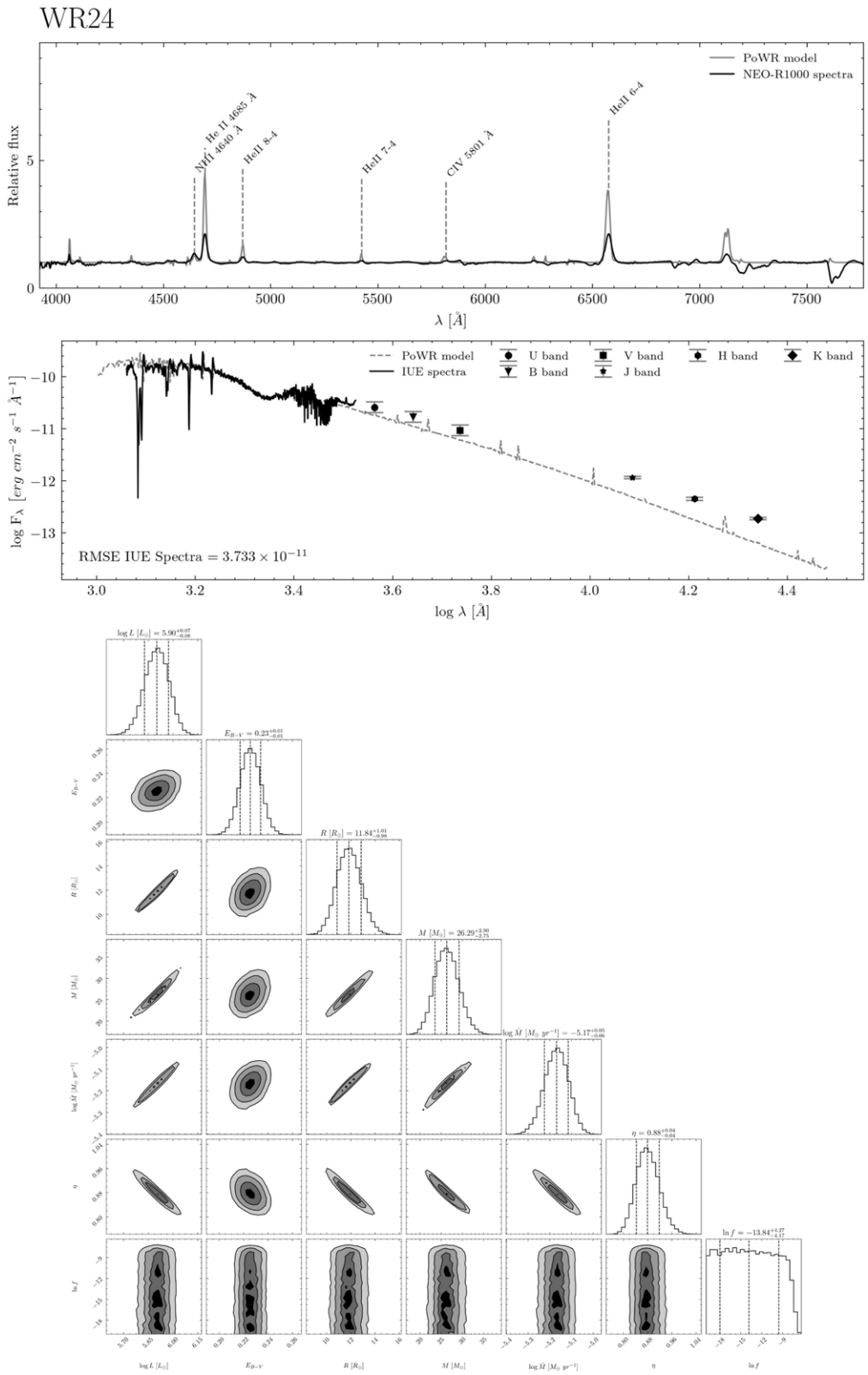

Figure A5. Fitting for WR24, same description as Figure A1.

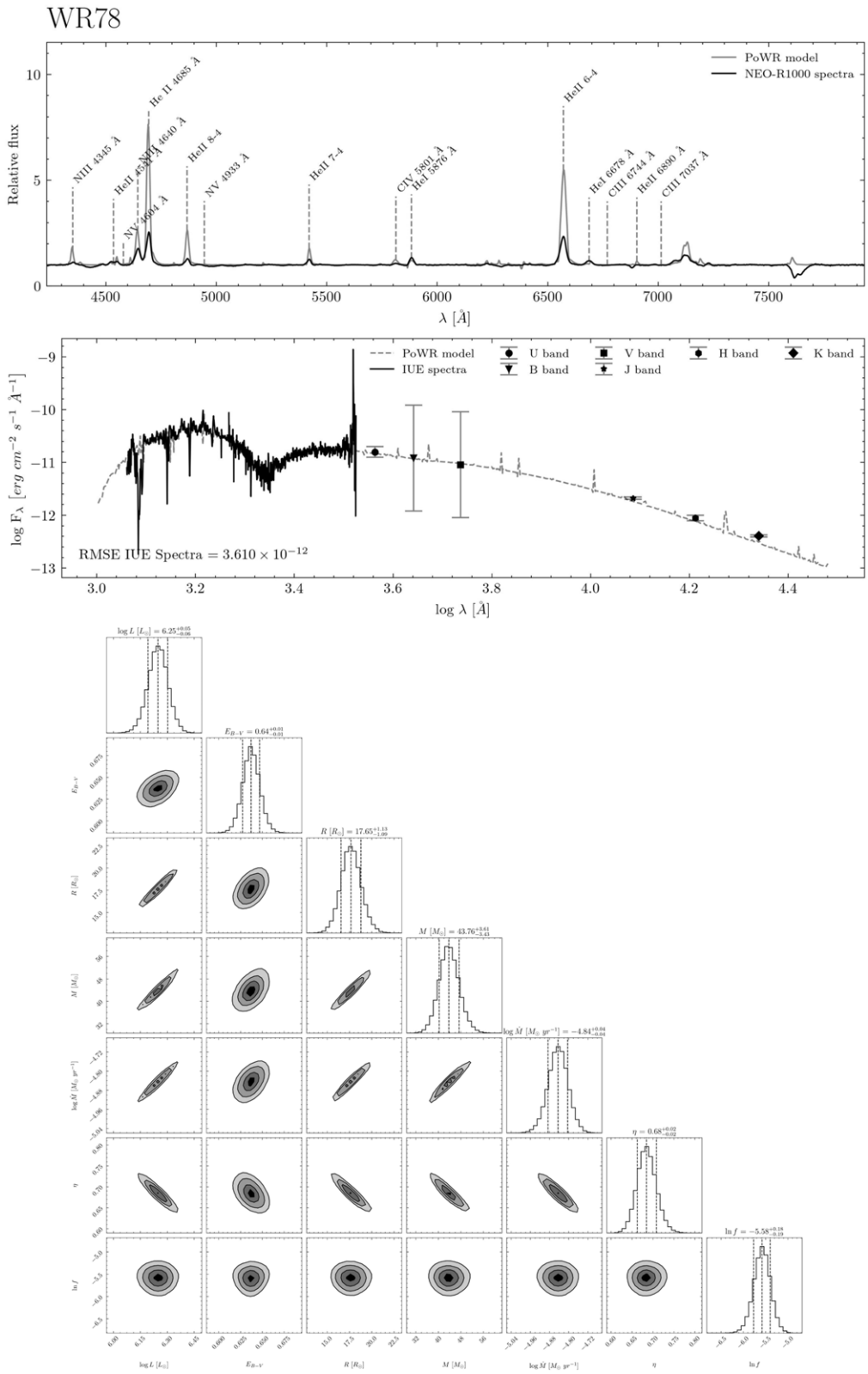

Figure A6. Fitting for WR78, same description as Figure A1.

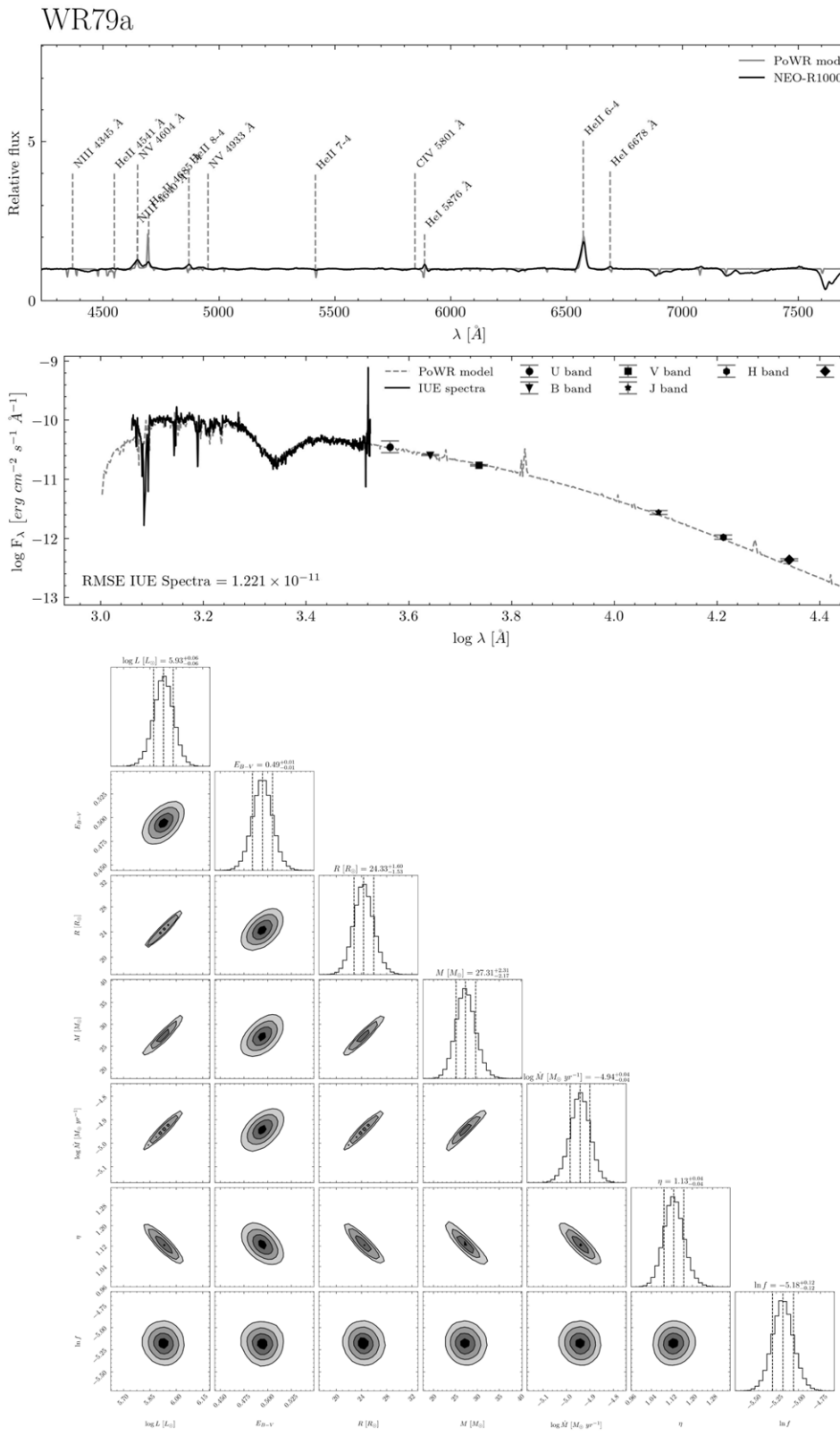

Figure A7. Fitting for WR79a, same description as Figure A1.

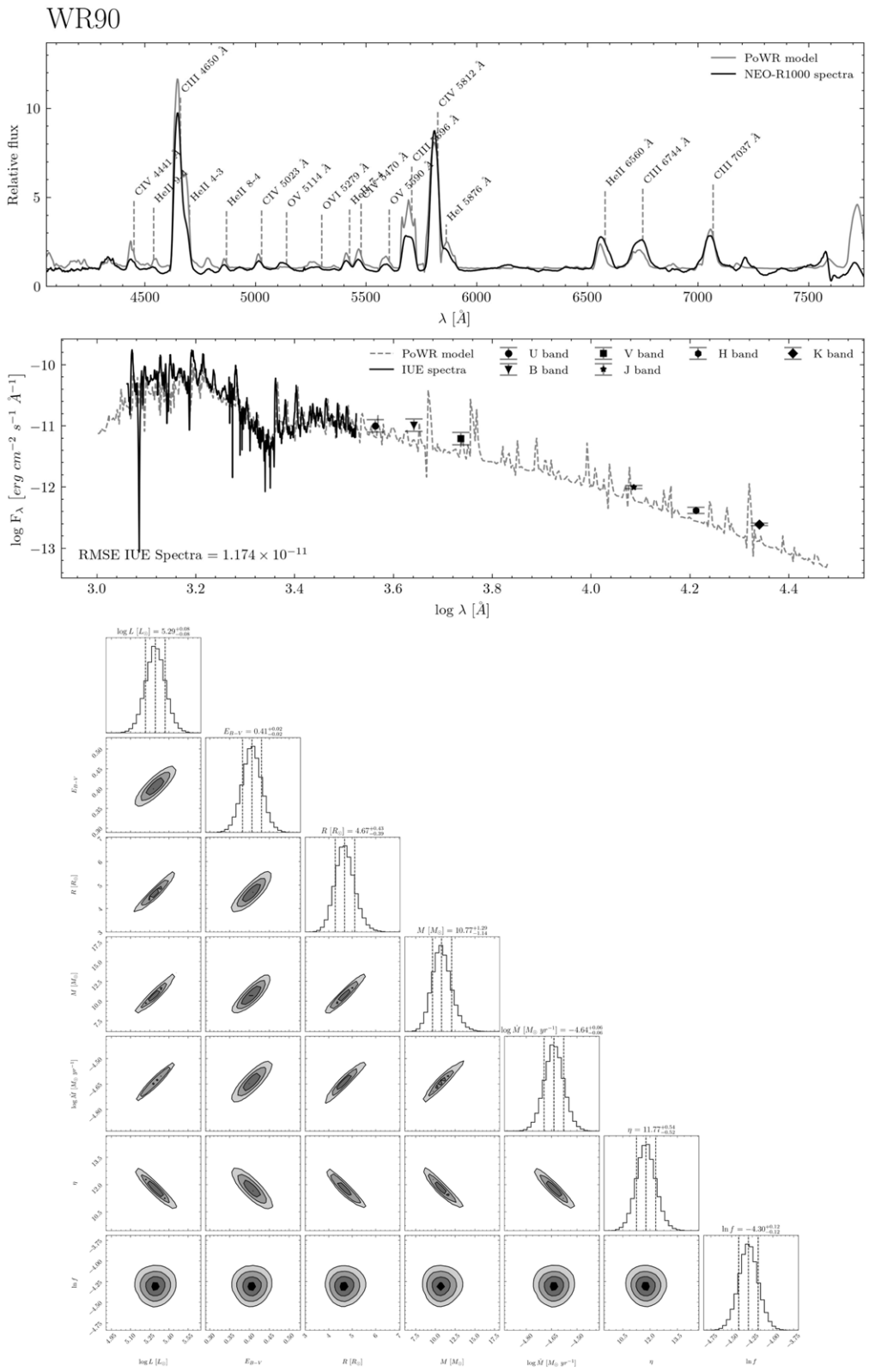

Figure A8. Fitting for WR90, same description as Figure A1.

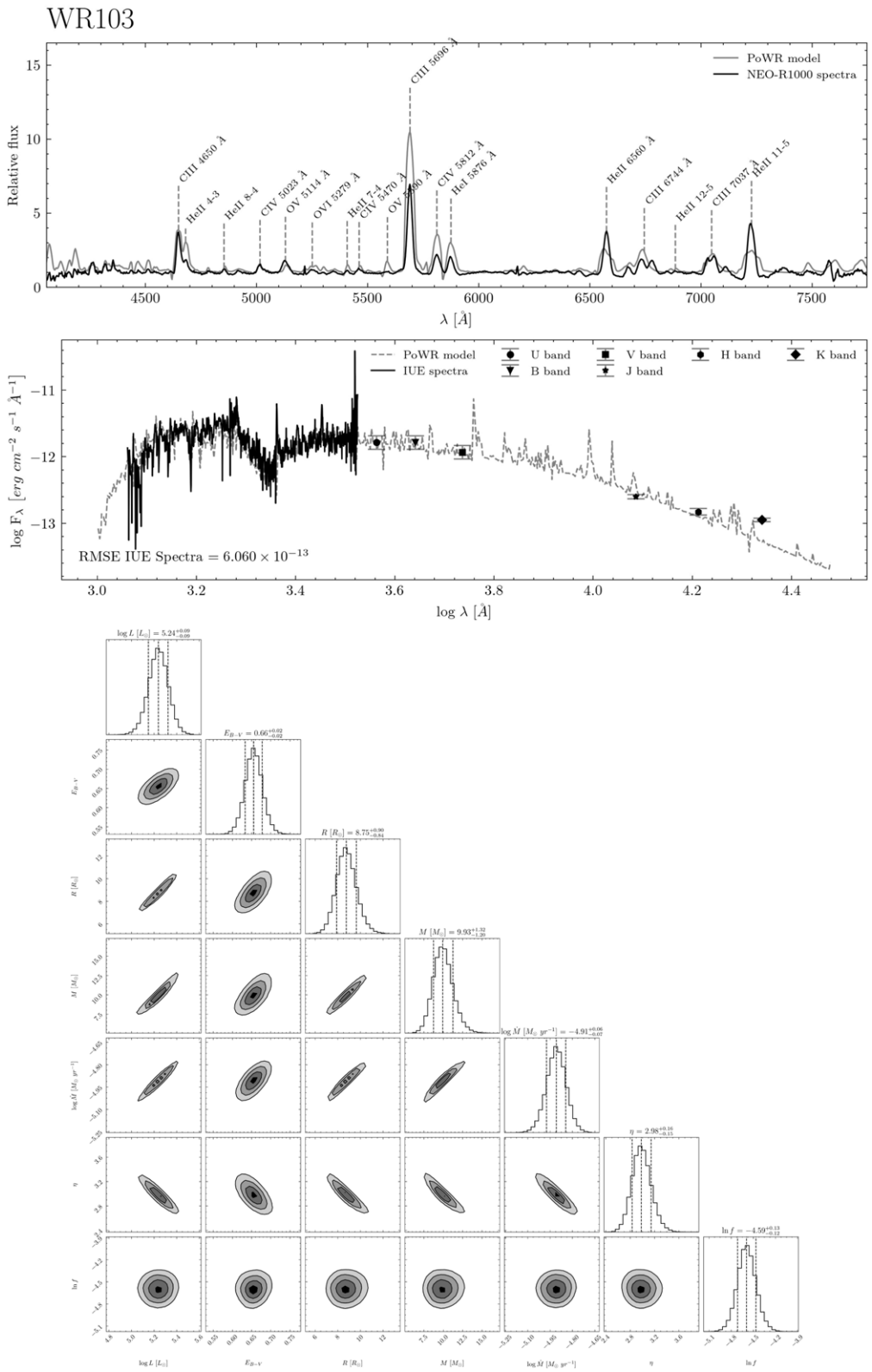

Figure A9. Fitting for WR103, same description as Figure A1.

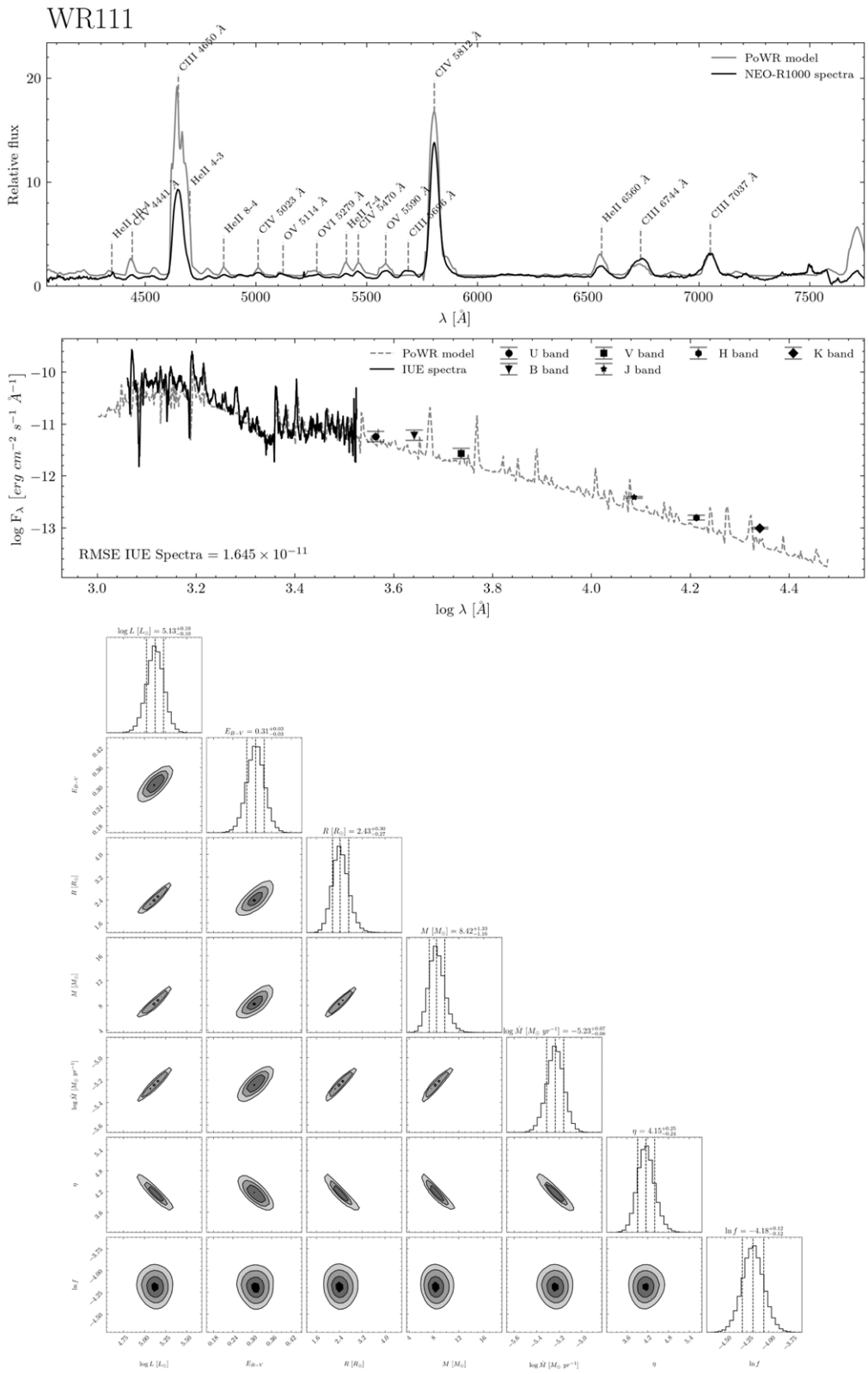

Figure A10. Fitting for WR111, same description as Figure A1.

Appendix B
P-Cygni Profile Analysis Results

Table B1
Velocity Measurement of Strong Ultraviolet P-Cygni Line Profiles

WR	Sp Type	v_∞ (km s^{-1})					
		N V $\lambda\lambda$1238.80 ,1242.80 ÅÅ	Si IV λ1393.75	Si IV λ1402.77	C IV $\lambda\lambda$1548.19 ,1550.76 ÅÅ	He II λ1640.40	N IV λ1718.55
WN							
6	WN4-s	2697(24)	…	…	2803(19)	1838(18)	1586(17)
24	WN6ha	3833(24)	1510(22)	1847(21)	2779(19)	1476(18)	1718(17)
78	WN7h	2925(24)	1178(22)	1396(21)	2000(19)	1123(18)	1952(17)
16	WN8h	…	1184(22)	1180(21)	1306(19)	753(18)	…
79a	WN9h	2643(24)	1406(21)	1326(21)	1599(19)	…	…
WC							
90	WC5	1971(22)	1557(22)	1769(21)	2841(19)	1869(18)	…
111	WC5	…	1319(22)	1899(21)	2313(19)	2037(18)	…
23	WC6	2047(22)	…	2167(21)	2757(19)	1983(18)	…
14	WC7	1757(22)	1532(22)	2295(21)	2208(19)	1930(18)	…
103	WC9d	1004(22)	1123(22)	1065(21)	1291(19)	669(18)	…

ORCID iDs

Hakim Luthfi Malasan https://orcid.org/0000-0001-8549-1811
Bakuh Danang Setyo Budi https://orcid.org/0009-0002-4853-9593

References

Adhyaqsa, A., Malasan, H. L., Aprilia, et al. 2020, JPhCS, 1523, 012001
Astropy Collaboration, Price-Whelan, A. M., Sipőcz, B. M., et al. 2018, AJ, 156, 123
Astropy Collaboration, Robitaille, T. P., Tollerud, E. J., et al. 2013, A&A, 558, A33
Boggess, A., Carr, F. A., Evans, D. C., et al. 1978, Natur, 275, 372
Boian, I., & Groh, J. H. 2018, A&A, 617, A115
Brethauer, D., Margutti, R., Milisavljevic, D., et al. 2022, ApJ, 939, 105
Bromage, G. E., van der Hucht, K. A., Macchetto, F., et al. 1982, in ESA Special Publication, Third European IUE Conference, ed. E. Rolfe & A. Heck, Vol. 176, 269
Cappa de Nicolau, C. E., Niemela, V. S., Dubner, G. M., et al. 1988, AJ, 96, 1671
Chené, A. N., & St-Louis, N. 2011, ApJ, 736, 140
Chiosi, C., & Maeder, A. 1986, ARA&A, 24, 329
Conti, P. S. 1975, MSRSL, 9, 193
Crowther, P. A. 2007, ARA&A, 45, 177
Crowther, P. A., De Marco, O., & Barlow, M. J. 1998, MNRAS, 296, 367
Crowther, P. A., Rate, G., & Bestenlehner, J. M. 2023, MNRAS, 521, 585
de la Chevrotière, A., St-Louis, N., Moffat, A. F. J. & MiMeS Collaboration 2013, ApJ, 764, 171
Dessart, L., Willis, A. J., Crowther, P. A., et al. 1999, in IAU Symp. 193, Wolf-Rayet Phenomena in Massive Stars and Starburst Galaxies, ed. K. A. van der Hucht, G. Koenigsberger, & P. R. J. Eenens (Berlin: Springer), 233
Ekström, S., Georgy, C., Eggenberger, P., et al. 2012, A&A, 537, A146
Fadeyev, Y. A. 2008, AstL, 34, 772
Foreman-Mackey, D., Hogg, D. W., Lang, D., et al. 2013, PASP, 125, 306
Garcia-Segura, G., & Mac Low, M.-M. 1995, ApJ, 455, 145
Georgy, C., Ekström, S., Meynet, G., et al. 2012, A&A, 542, A29
González-Riestra, R., Cassatella, A., Solano, E., et al. 2000, A&AS, 141, 343
Gordon, K. D., Fouesneau, M., Arab, H., et al. 2016, ApJ, 826, 104
Gräfener, G., Koesterke, L., & Hamann, W. R. 2002, A&A, 387, 244
Hamann, W. R., & Gräfener, G. 2003, A&A, 410, 993
Hamann, W. R., Gräfener, G., & Liermann, A. 2006, A&A, 457, 1015
Hamann, W. R., Gräfener, G., Liermann, A., et al. 2019, A&A, 625, A57
Hidayat, B. 1995, JApAS, 16, 301
Hidayat, B., Supelli, K., & van der Hucht, K. A. 1982, in IAU Symp. 99, Wolf-Rayet Stars: Observations, Physics and Evolution, ed. C. W. H. De Loore & A. J. Willis (Berlin: Springer), 27
Hillier, D. J. 2020, Galax, 8, 60
Kogure, T., & Leung, K.-C. 2007, The Astrophysics of Emission-Line Stars, Vol. 342 (New York: Springer)
Langer, N. 1989, A&A, 210, 93
Lenoir-Craig, G., St-Louis, N., Moffat, A. F. J., et al. 2022, ApJ, 925, 79
Lundstrom, I., & Stenholm, B. 1984, A&A, 138, 311
Malasan, H. L., Jihad, I., Muztaba, R., et al. 2016, Indonesian J. Phys., 27, 1
Malasan, H. L., Prabowo, D. A., Adhyaqsa, A., et al. 2020, E&ES, 537, 012008
Malasan, H. L., & Raharto, M. 1993, in 5th Int. Sym. on Equatorial Atmospheric Observation over Indonesia (BPPT), 33
Margutti, R., Kamble, A., Milisavljevic, D., et al. 2017, ApJ, 835, 140
Massey, P., Lundstrom, I., & Stenholm, B. 1984, PASP, 96, 618
Meynet, G., Maeder, A., Schaller, G., Schaerer, D., & Charbonnel, C. 1994, A&AS, 103, 97
Niedzielski, A., & Skorzynski, W. 2002, AcA, 52, 81
Nugis, T., & Lamers, H. J. G. L. M. 2000, A&A, 360, 227
Prinja, R. K., Barlow, M. J., & Howarth, I. D. 1990, ApJ, 361, 607
Prinja, R. K., Barlow, M. J., & Howarth, I. D. 1991, ApJ, 383, 466
Prša, A., Harmanec, P., Torres, G., et al. 2016, AJ, 152, 41
Rate, G., & Crowther, P. A. 2020, MNRAS, 493, 1512
Rustamov, J. N. 2017, AJAz, 12, 15
Sander, A. A. C., Hamann, W. R., Todt, H., et al. 2019, A&A, 621, A92
Sander, A., Hamann, W. R., & Todt, H. 2012, A&A, 540, A144
Sander, A., Shenar, T., Hainich, R., et al. 2015, A&A, 577, A13
Sasaki, M., Robrade, J., Krause, M. G. H., et al. 2024, A&A, 682, A172
Shylaja, B. S. 1990, Ap&SS, 164, 63
Skinner, S. L., Zhekov, S. A., Güdel, M., Schmutz, W., & Sokal, K. R. 2012, AJ, 143, 116
Smith, L. F., Shara, M. M., & Moffat, A. F. J. 1996, MNRAS, 281, 163
Springmann, U. 1994, A&A, 289, 505
Toalá, J. A., & Guerrero, M. A. 2013, A&A, 559, A52
Todt, H., Sander, A., Hainich, R., et al. 2015, A&A, 579, A75
van der Hucht, K. A. 2001, NewAR, 45, 135
Welsh, B. Y., Sallmen, S., Jelinsky, S., & Lallement, R. 2003, A&A, 403, 605
Willis, A. J., & Wilson, R. 1977, A&A, 59, 133
Willis, A. J., & Wilson, R. 1978, MNRAS, 182, 559